J. Fluid Mech. (1977), *vol.* 82, *part* 3, *pp.* 583–604
Printed in Great Britain

An approximate theory for the streaming motion past axisymmetric bodies at Reynolds numbers of from 1 to approximately 100

By MICHAEL S. KOLANSKY, SHELDON WEINBAUM AND ROBERT PFEFFER

The City College of the City University of New York

(Received 4 August 1976)

In Weinbaum *et al.* (1976) a simple new pressure hypothesis is derived which enables one to take account of the displacement interaction, the geometrical change in streamline radius of curvature and centrifugal effects in the thick viscous layers surrounding two-dimensional bluff bodies in the intermediate Reynolds number range $O(1) < Re < O(10^2)$ using conventional Prandtl boundary-layer equations. The new pressure hypothesis states that the streamwise pressure gradient as a function of distance from the forward stagnation point on the displacement body is equal to the wall pressure gradient as a function of distance along the original body. This hypothesis is shown to be equivalent to stretching the streamwise body co-ordinate in conventional first-order boundary-layer theory. The present investigation shows that the same pressure hypothesis applies for the intermediate Reynolds number flow past axisymmetric bluff bodies except that the viscous term in the conventional axisymmetric boundary-layer equation must also be modified for transverse curvature effects $O(\delta)$ in the divergence of the stress tensor. The approximate solutions presented for the location of separation and the detailed surface pressure and vorticity distribution for the flow past spheres, spheroids and paraboloids of revolution at various Reynolds numbers in the range $O(1) < Re < O(10^2)$ are in good agreement with available numerical Navier–Stokes solutions.

1. Introduction

In an earlier paper by the authors (Weinbaum *et al.* 1976, hereafter referred to as WKPG) a new approximate theory was presented for the two-dimensional flow past smoothly contoured bluff objects in the intermediate Reynolds number regime $O(1) < Re < O(10^2)$, where the viscous displacement of the outer flow produced by the body boundary layer and wake is of comparable magnitude to that produced by the original body and centrifugal effects in the thick viscous layer enshrouding the body cannot be neglected. For finite bodies the upper limit of validity of the new approximate theory is determined by the condition that the wake separation bubble behind the body be steady and laminar. This limit has been experimentally observed to occur at Reynolds numbers of approximately 60 for circular cylinders and 130 for spheres (Batchelor 1967, p. 51). For semi-infinite bodies without separation the new theory provides a smooth transition to the solutions obtained from Prandtl's classical high Reynolds number laminar boundary-layer theory.

Flows in the intermediate Reynolds number regime of interest in the present study have long defied simpler theoretical treatment. Theoretical approaches from the low Reynolds number end of the regime, which have been based on Oseen-type linearizations, have not proved fruitful for $Re > O(1)$ because of the inability of an approximation linear in the velocity to describe adequately the separation and wake-formation phenomena on bluff bodies. Theoretical approaches from the upper end of the intermediate Reynolds number range have been based largely on the concepts of higher-order boundary-layer theory (Van Dyke 1962). This theory similarly breaks down because it is a successive approximation scheme based on the potential flow past the original body, which in general will depart substantially from the effective displacement body with its wake at these Reynolds numbers.

At the heart of the new intermediate Reynolds number theory for axisymmetric flow described herein is a new simplifying pressure hypothesis derived in WKPG that approximately relates the pressure gradients along the surfaces of the original body and the effective displacement body when centrifugal forces and viscous displacement interaction are considered. Earlier numerical studies by Gluckman (1971) and Werle & Worman (1972) had demonstrated that, if either experimentally measured or numerically generated Navier–Stokes surface pressure distributions were used to drive the Prandtl boundary-layer equations, good predictions of the separation-point location and the surface vorticity distribution were possible for the flow past a circular cylinder for the entire range of Reynolds numbers where a steady wake separation bubble exists. This suggested that conventional boundary-layer equations were still an adequate description of the growth of the viscous layer provided that the surface pressure boundary condition was modified to take account of the centrifugal forces that were omitted from the boundary-layer equations, the approximate change in radius of curvature of the streamlines as one moves outwards along a normal to the body surface, and the effective enlargement of the body as seen by the inviscid outer flow. Thus the fundamental question asked in WKPG was whether one could generate, using the Prandtl boundary-layer equations, a displacement body which had a pressure gradient along its surface which was the same as the pressure gradient obtained from a higher-order approximation to the Navier–Stokes equations [WKPG, equations (2) and (3)] in which centrifugal forces and the normal variation in streamline curvature were retained. This effective pressure gradient would act through the centroid of vorticity (Lighthill 1958) of the local velocity profile and produce the same displacement-thickness distribution as the higher-order set of equations.

In answer to the question just posed, it is shown in WKPG that the streamwise pressure gradient $\partial p/\partial s^*$ along the displacement surface obtained using Prandtl boundary-layer theory and the conventional construction of the displacement body will be equal to the streamwise pressure gradient along the displacement body obtained by integrating a higher-order approximation to the Navier–Stokes equations [WKPG, equations (2) and (3)] in which centrifugal forces and the normal pressure field are included provided that

$$\frac{\partial p}{ds_w} = \left(\frac{R_w}{R^*}\right)\frac{\partial p}{\partial s_{wn}} - \frac{1}{Re^{\frac{1}{2}} R_w R^*}\left(\frac{\partial R_w}{\partial s_w}\right)\int_0^{n^*} u^2 dn. \tag{1}$$

Equation (1) relates the wall pressure gradient in the Prandtl boundary-layer equation

dp/ds_w to the wall pressure gradient $\partial p/\partial s_{wn}$ in the higher-order approximation to the Navier–Stokes equations for the flow past the original body. Here Re is a characteristic Reynolds number based on the free-stream velocity and body dimensions, s and n are streamline and normal co-ordinates scaled by a characteristic boundary-layer thickness δ_0, R_w and R^* are the local radii of curvature of the wall and the displacement body and the asterisks denote conditions at the displacement surface. The first term in (1) is a centrifugal correction due to the increase in streamline radius of curvature as one proceeds away from the wall while the second term arises from the streamwise variation in curvature of the wall itself. Since s is scaled by δ_0 (see WKPG for a further discussion of this point), the second term in (1) will, in general, be small compared with the first unless R_w changes to lowest order on a length scale $O(\delta_0)$. For a sphere this term is identically zero. Thus for smoothly contoured bodies without sharp corners (1) reduces to

$$\frac{dp}{ds_w} = \frac{\partial p}{\partial s_{wn}}\left(\frac{R_w}{R^*}\right) = \frac{dp}{ds^*}, \tag{2}$$

where in the second equality we have used the approximation that $ds^* = (R^*/R_w)\,ds_{wn}$, and where, in defining ds^*, we have assumed that the streamlines are locally parallel to the body so that the local radius of curvature of the streamlines can be approximated by $R = R_w + Re^{-\frac{1}{2}}n$.

Equation (2) states that if the Prandtl boundary-layer equations are used to generate a displacement body in which viscous-layer centrifugal effects are included then, except for a constant of integration, the pressure as a function of distance along the surface of the original body should be equal to the pressure as a function of distance along the displacement body. The pressure transformation from the displacement body back to the surface of the original body is thus one that preserves arc length, i.e. $ds_w = ds^*$. This pressure mapping is equivalent to stretching the differential distance element along the body surface by a factor R^*/R_w in the expression for the wall pressure gradient.

The principal simplifying assumptions used in the derivation of (1) and (2) are that the local radius of curvature of the displacement body is equal to the local radius of curvature of the original body plus the local displacement thickness and that viscous corrections to the normal pressure field are $O(Re^{-1})$ and can therefore be neglected. The basic difference between the two-dimensional analysis presented in WKPG and the axisymmetric theory described herein is the presence of transverse curvature effects in the continuity equation and the viscous terms of the streamwise momentum equation. These differences affect the normal pressure field only to $O(Re^{-1})$ and have been omitted.

The new pressure hypothesis has been tested against a wide variety of two-dimensional numerical Navier–Stokes solutions in WKPG. Remarkably good agreement was obtained after a single iteration for the surface pressure distribution for both semi-infinite and finite bodies (parabolas and circular and elliptic cylinders) over the entire range of Reynolds numbers where these finite-difference solutions exist. Equally good agreement is obtained in the present study for the flow past paraboloids of revolution, spheres and spheroids.

The other novel feature of the new approximate theory is the successive approximation scheme used for determining the inner and outer flow solutions when both

the surface pressure distribution and the effective displacement body are unknown. Owing to the large distortion in the effective body shape caused by the thick viscous layers and wake, one seeks an iterative solution procedure in which the initial guess for the surface pressure distribution already takes into account in an approximate manner the displacement and centrifugal effects of the viscous flow region. The first trial solution for the potential-flow pressure distribution is thus based on a family of enlarged geometrically similar bodies whose local radius increases in accordance with the growth of the viscous displacement thickness up to the station in question, the surface pressure gradient being modified to satisfy the new pressure hypothesis (2). The solution for the outer flow for second- and higher-order iterations is complicated by the fact that it requires a potential-flow solution for the flow past a boundary of arbitrary symmetric shape. Accurate but approximate solution techniques based on the boundary method have been developed in WKPG for two-dimensional potential flow. These techniques, which differ for finite and semi-infinite bodies, are extended in the present study to axisymmetric potential flows.

This extended introduction has been given to provide continuity between the present investigation and the earlier two-dimensional study. Much of the theoretical development for axisymmetric flow parallels that already presented in WKPG. Only the important differences in this development will be presented in detail herein. The reader is referred to this earlier work for a more complete description of the basic solution procedure and discussion of the fundamental simplifying assumptions.

Section 2 states the boundary-value problems for the viscous and inviscid flow regions. The general solution procedure is briefly summarized in §3. Sections 4, 5 and 6 describe the application of the new displacement interaction model to paraboloids of revolution, spheres and prolate spheroids and present detailed numerical comparisons with existing exact Navier–Stokes solutions for the flow past these bodies.

2. The boundary-value problem for axisymmetric flow

In accord with the foregoing discussion, the governing equations for the thick viscous layers are the conventional axisymmetric boundary-layer equations correct to $O(\delta_0)$ with the streamwise pressure gradient modified in accordance with the new pressure hypothesis (2). These equations differ from the lowest-order Prandtl boundary-layer equations for two-dimensional flow in that the streamwise momentum and continuity equations contain viscous corrections $O(\delta_0)$, first derived by Millikan (1932), which arise from transverse-curvature contributions to the divergence of the stress tensor and velocity field respectively. The equations in question are

$$u\frac{\partial u}{\partial x}+v\frac{\partial u}{\partial y}=-\frac{1}{\rho}\frac{dp}{dx}+\nu\left(\frac{\partial^2 u}{\partial y^2}+\frac{1}{R}\frac{\partial R}{\partial y}\frac{\partial u}{\partial y}\right), \tag{3}$$

$$\partial/(uR)/\partial x+\partial(vR)/\partial y = 0. \tag{4}$$

Here R is related to the normal boundary co-ordinate y (see figure 1) by

$$R = R_0+y\cos\epsilon \tag{5}$$

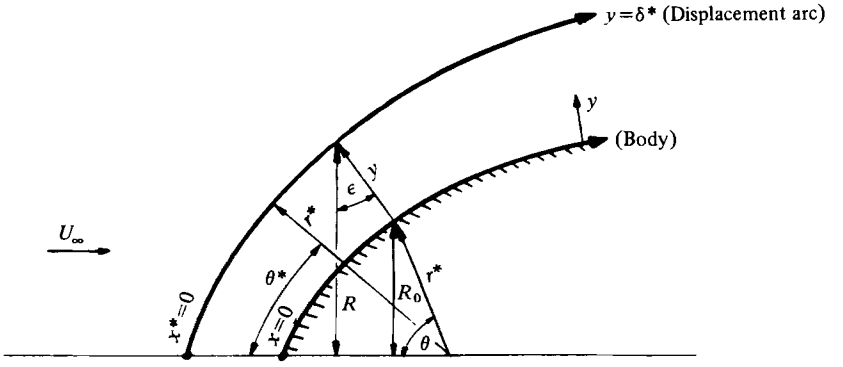

FIGURE 1. Boundary-layer co-ordinate system.

and from (2) the wall pressure gradient dp/dx is given by

$$dp/dx = dp/dx^*, \tag{6a}$$

with

$$x = x^*. \tag{6b}$$

Here x^* is the distance s^* measured from the forward stagnation point of the displacement body

One observes that, in the limit $R \to \infty$, (3) reduces to the classical two-dimensional equation given by Prandtl, whereas for $\epsilon = \frac{1}{2}\pi$, (3) and (4) reduce to the governing equations for an axisymmetric stagnation-point flow. From (6) the pressures as functions of distance along the original and displacement bodies respectively are equal except for an additive constant due to viscous losses in total pressure along the streamline passing through the forward stagnation point. Since $r^* > r_w$ the local polar co-ordinate θ is stretched such that $\theta > \theta^*$ as shown in figure 1.

The effective displacement body is constructed by adding to the original body surface the displacement-thickness distribution

$$\delta^*(x) = \frac{1}{U(x)}\int_0^{\delta(x)} (U(x)-u)\,dy \tag{7}$$

obtained from the solution of (3) for the velocity profile. This differs from the conventional method of constructing the displacement body in that the inviscid pressure gradient at a position x^* (angular location θ^*) on the displacement surface is used to calculate the displacement thickness δ^* at a position x (angular location θ) on the original body in accord with the pressure mapping described by (6).

The inviscid pressure distribution and the velocity $U(\theta^*)$ at the surface of the displacement body are determined from the solution of the generalized axisymmetric potential-flow equation

$$D^2\psi = 0, \tag{8}$$

where ψ is the inviscid stream function. This equation satisfies the usual inviscid boundary condition that the normal component of the velocity vanishes at the displacement surface:

$$v(x^*) = 0 \quad \text{on} \quad r = r^*. \tag{9}$$

Since the solution for $\delta^*(x)$ depends on the solution for $p(x)$ and both are unknown, the solution of (3)–(9) represents a coupled nonlinear boundary-value problem. In

essence, we wish to solve (8) subject to a known boundary condition (9) along an unknown surface, the effective displacement body. This body is determined from the solution of (3) and (4), in which the surface pressure distribution satisfies the pressure hypothesis (6) and must be obtained through a process of iterative approximation.

3. Solution procedure

The solution procedure developed for solving the boundary-value problem presented in §2 is basically the same as that described in detail in WKPG for the two-dimensional case. Below we shall only summarize the method for generating the first trial solution for the displacement body and the iteration procedure for obtaining a converged solution and refer the reader to WKPG for the motivation and rationale behind the development of the solution techniques.

3.1. *First trial solution for the displacement body*

(1) Both the displacement thickness and the pressure gradient at the forward stagnation point are unknown. To approximate the displacement body a family of geometrically similar bodies with the same focal point as the original body is selected. The pressure or velocity gradient at the forward stagnation point on the displacement body is written in terms of the unknown displacement thickness and applied at the surface of the original body using the pressure-stretching hypothesis (6). This expression is then solved simultaneously with (3) applied at the forward stagnation point. The solution technique is illustrated in § 3.3 for the case of a sphere.

(2) Having obtained this first trial solution for δ^*, dp/dx and the velocity profile at the forward stagnation point, one performs a forward numerical integration of (3). For present purposes it was deemed satisfactory to use a momentum-integral approximation to (3) rather than the more accurate finite-difference solutions in view of the other approximations introduced. At each forward integration step the pressure gradient is represented by the local pressure gradient for inviscid flow past the geometrically similar body whose local radius from the focal point of the original body is equal to that of the displacement body. From (6) this pressure gradient is also the pressure gradient along the original body surface.

(3) The displacement-thickness distribution obtained from the solution described in step 2 is now added on normally to the surface of the original body. Because of the pressure mapping (6*b*) the pressure gradient at a position x^* on the displacement body is used to calculate the displacement thickness at the position $x = x^*$ on the original body as shown in figure 1. This completes the first trial solution for the effective displacement body.

3.2. *The iteration procedure for a converged solution*

(1) As we shall observe in the results, the first trial solution just outlined provides a reasonable approximation to the displacement surface since it qualitatively includes the streamwise co-ordinate straining required to describe curvature effects. However, it provides a poor detailed description of the surface pressure distribution since the actual shape of the displacement body and its wake can depart significantly from the family of geometrically similar bodies used in the first trial solution. The first step

towards obtaining a converged solution is thus to obtain a much more accurate representation of the potential-flow pressure distribution on the displacement body. This task is equivalent to solving (8) and (9) for an arbitrary boundary shape, since the displacement body obtained in § 3.1 will not in general have a simple analytic representation. An approximate combined numerical and analytical solution technique based on the boundary method has been developed for this purpose and is described in § 3.4.

(2) The potential-flow pressure distribution on the first-order displacement body obtained in step 1 is now mapped back to the surface of the original body using (6*b*). The momentum-integral-equation form of (3) is then solved again using this new pressure distribution.

(3) The new solution for the displacement-thickness distribution found in step 2 is now added on normally to the surface of the original body, in the same manner as before, to obtain the second-order approximation to the displacement body.

(4) Steps 1–3 are now repeated to obtain the third- and higher-order approximations to the displacement body until convergence in either the body shape or the surface pressure distribution is achieved to within predetermined limits.

In accord with the preceding solution outline the approximate equation for the viscous layer is the momentum-integral equation obtained from (3) and (4). This equation can be derived either by a direct integration of (3) and (4) (Millikan 1932) or by using a control-volume approach (Gluckman 1971). The desired equation is

$$\frac{d\theta}{dx} = \frac{(\Lambda\nu U'_e)^{\frac{1}{2}}}{Ue}\left(\frac{2}{\Lambda}+\frac{1}{6}-\frac{2\theta}{\delta}-\frac{\delta^*}{\delta}-\frac{R'}{R}\frac{U_e}{U'_e}\frac{\theta}{\delta}-\frac{\gamma F_1}{RU_e(\Lambda\nu U'_e)^{\frac{1}{2}}}-\frac{\gamma' F_2}{RU_e(\Lambda\nu U'_e)^{\frac{1}{2}}}\right), \tag{10}$$

where

$$\delta^* = \frac{1}{U_e}\int_0^\delta (U_e-u)\,dy, \quad \text{the displacement thickness,} \tag{11a}$$

$$\theta = \frac{1}{U_e^2}\int_0^\delta u(U_e-u)\,dy, \quad \text{the momentum thickness,} \tag{11b}$$

$$\Lambda = \frac{\delta^2}{\nu}\frac{dU_e}{dx}, \quad \text{the velocity-profile shape factor,} \tag{12a}$$

$$\gamma = [1-(dR/dx)^2]^{\frac{1}{2}}, \tag{12b}$$

$$F_1 = d[(A_2-A_1)\,U_e^2\delta^2]/dx+(\tfrac{1}{2}-A_2)\,U_eU'_e\delta^2, \tag{12c}$$

$$F_2 = (A_2-A_1)\,U_e^2\delta^2, \tag{12d}$$

$$A_1 = \frac{e^2}{4}+\frac{2ef}{5}+\frac{(f^2+2eg)}{6}+\frac{2(eh+fg)}{7}+\frac{(g^2+2gh)}{8}+\frac{2gh}{9}+\frac{h^2}{10}, \tag{12e}$$

$$A_2 = \frac{e}{3}+\frac{f}{4}+\frac{g}{5}+\frac{h}{6}. \tag{12f}$$

Equation (10) would be identical to the integral form of the high Reynolds number axisymmetric boundary-layer equation were it not for the last two terms in the bracket on the right side. These two terms represent transverse-curvature effects

$O(\delta_0)$. The coefficients e, f, h and h in (12) are derived from the Pohlhausen quartic profile

$$\frac{U}{U_e} = e\left(\frac{y}{\delta}\right) + f\left(\frac{y}{\delta}\right)^2 + g\left(\frac{y}{\delta}\right)^3 + h\left(\frac{y}{\delta}\right)^4 \tag{13}$$

with

$$e = 2+\frac{\Lambda}{6}, \quad f = -\frac{\Lambda}{2}, \quad g = -2+\frac{\Lambda}{2}, \quad h = 1-\frac{\Lambda}{6}. \tag{13a–d}$$

This profile provides a reasonable description up to separation and a solution of undetermined accuracy beyond the separation point. One notes, however, that the smoothly varying polynomial profile is more likely to provide at least a qualitatively realistic description of the separated flow at the intermediate Reynolds numbers considered herein, where steep vorticity gradients are not present, than at high Re, where there is a thin boundary-layer-like structure both in the reversed flow near the wall and in the separated free shear layers.

The ratios θ/δ and δ^*/δ are given for completeness:

$$\frac{\theta}{\delta} = \frac{1}{63}\left(\frac{37}{5} - \frac{\Lambda}{15} - \frac{\Lambda^2}{144}\right), \tag{14a}$$

$$\frac{\delta^*}{\delta} = \frac{3}{10} - \frac{\Lambda}{120}. \tag{14b}$$

3.3. *First trial solution for the forward stagnation point*

To elucidate the solution procedure described under step 1 in §3.1, we consider the stagnation-point flow on a sphere of unit radius. The geometrically similar displacement bodies considered are concentric spheres of radius $r^* = 1+\delta^*$. Both δ^* and dU/dx at the forward stagnation point are unknown. The potential-flow solution for the velocity on the surface of a geometrically similar displacement sphere of radius r^* is

$$U_e = \tfrac{3}{2}U_\infty \sin\theta^*, \tag{15}$$

where θ and θ^* are related by $r\theta = r^*\theta^*$ from (6b). The velocity gradient at the forward stagnation point on the original body surface obtained from (15) and the pressure transformation (6) is

$$\frac{dU_e}{dx} = \frac{\frac{3}{2}U_\infty}{1+\delta^*}\cos\theta^*. \tag{16}$$

Both δ^* and U_e' are unknown at the forward stagnation point. The solution of (10) at the forward stagnation point requires that

$$\frac{2}{\Lambda} + \frac{1}{6} - \frac{2\theta}{\delta} - \frac{\delta^*}{\delta} - \left(\frac{R'}{R}\right)\left(\frac{U_e}{U_e'}\right)\frac{\theta}{\delta} - \frac{\gamma F_1 + \gamma' F_2}{RU_eU_e'\delta} = 0. \tag{17}$$

Inserting the definitions (12) and (13) into (17) one obtains an expression for the velocity-profile shape factor Λ at the forward stagnation point:

$$\Lambda_{\mathrm{fsp}} = 2\Big/\left[\left(2+\frac{1}{R}\right)\frac{\theta}{\delta} + \frac{\delta^*}{\delta} + \frac{\delta}{R}\left(2A_2 - 3A_1 + \frac{1}{2}\right) - \frac{1}{6}\right]. \tag{18a}$$

Equation (18a) is an interesting new result because it shows that the effect of the transverse-curvature terms in (10) is to make the shape factor and hence the velocity

Reynolds number	Λ_{fsp}
∞	4·7160
130	4·318933
100	4·271017
60	4·163813
40	4·064817
15	3·772365
10	3·631787
8	3·54948
5	3·36939

TABLE 1. Λ_{fsp} for various Reynolds numbers for a sphere.

profile at the forward stagnation point a function of Reynolds number in contrast to the two-dimensional stagnation-point solution considered in WKPG. Table 1 shows the results for Λ_{fsp} for various Reynolds numbers based on sphere diameter. As can be seen from table 1 the results for large Reynolds numbers asymptotically approach the high Reynolds number, boundary-layer result Λ_{fsp} = constant = 4·716.

The displacement thickness at the forward stagnation point can be calculated from

$$\delta^*(0) = \frac{G}{2Re} + \left(\frac{G^2}{4Re^2} + \frac{G}{Re}\right)^{\frac{1}{2}}, \tag{18b}$$

where

$$G = \frac{4\Lambda_{fsp}}{3}\left(\frac{3}{10} - \frac{\Lambda_{fsp}}{120}\right)^2. \tag{18c}$$

$\delta^*(0)$ thus depends on the Reynolds number and the body geometry.

3.4. *Inviscid flow past the displacement body*

The crucial step in the iterative approximation procedure used to obtain a converged solution is the development of a simple yet accurate approximate technique for determining the flow past smoothly contoured non-analytic boundary shapes. In our earlier work (WKPG) an approximate technique was developed for two-dimensional potential flows in which the displacement body (including the wake) was represented by an internal distribution of line sources and sinks whose strengths and locations were determined using a boundary-method approach in which inviscid boundary conditions are satisfied at discrete points on the body. The detailed application of the boundary method developed differed depending on whether the aspect ratio of the body was low or high (this included semi-infinite bodies). Following this earlier development one now starts with an unknown finite distribution of N point sources and sinks of strengths m_i located at positions x_i along the axis of symmetry of the body and placed in a uniform stream. The stream function for this flow which satisfies (8) is

$$\psi = -U_\infty R^2 + \sum_{i-1}^{\infty} m_i \left(\frac{x - x_i}{[(x-x_i)^2 + R^2]^{\frac{1}{2}}} - 1\right), \tag{19}$$

where (x, R) here represent cylindrical polar co-ordinates. For the flow past bodies of low and moderate aspect ratio, such as a sphere, one finds that a surprisingly good representation of the desired $\psi = 0$ boundary shape can be obtained using only four

equally spaced boundary points between flow attachment and separation if both m_i and x_i are left unspecified and the series in (19) is truncated at $N = 2$. The accuracy of this simple representation will be discussed later in connexion with figures 3(*a*) and (*b*).

For the flow past semi-infinite bodies, such as the family of paraboloids of revolution considered herein, or finite bodies of high aspect ratio, many more boundary points are required for an accurate curve fit in which the $\psi = 0$ streamline does not exhibit wavelike undulations. The solution of the matrix of equations derived from (19) when many boundary points are required is extremely tedious if both m_i and x_i are treated as unknowns, since the x_i appear nonlinearly. A much simpler procedure for these extended bodies is to specify the source–sink locations x_i and leave only the values of m_i to be determined, since these constants appear linearly in (19). A convenient but arbitrary selection of boundary points and source locations in this procedure is to position the singularities directly below the boundary points in one-to-one correspondence. Employing standard matrix reduction schemes for systems of linear equations, one can easily handle as many as 100 boundary points using less than a second of computer time.

4. Paraboloids of revolution

As the first application of the new approximate theory described in §§2 and 3, we consider the uniform viscous flow past axisymmetric paraboloids of revolution whose surface is defined by

$$R^2 = 4(1+x) \tag{20}$$

at various Reynolds numbers. This simple body shape, for which separation does not occur, provides a convenient axisymmetric geometry to test the basic hypothesis of the new model with existing finite-difference solutions of the Navier–Stokes equations (Davis & Werle 1972) and conventional boundary-layer theory.

The family of geometrically similar axisymmetric paraboloids used to generate the surface pressure distribution in (10) for the construction of the first guess for the displacement body is given by

$$R^2 = 4c^2(x+c^2). \tag{21}$$

For $c = 1$ this reduces to (20) whereas for $c > 1$ one obtains a family of geometrically enlarged paraboloids with a common focal point at the origin.

The speed along the surface of the paraboloid defined by (21) is

$$q = U = U_\infty \cos \tfrac{1}{2}(\pi - \theta^*). \tag{22}$$

The potential-flow solution (22) replaces (15) in the first trial solution for the flow at the forward stagnation point and is also used to approximate the local pressure gradient in (10) as described in step 2 of the procedure for determining the first trial solution for the displacement body. In applying the pressure mapping (6) we have related the polar angles θ and θ^* measured from the forward stagnation point along the surfaces of the original body and the effective displacement body by the arc-length formula

$$\int_0^{\theta^*} \left[r^{*2} + \left(\frac{dr^*}{d\theta}\right)^2\right]^{\frac{1}{2}} d\theta = \int_0^{\theta} \left[r^2 + \left(\frac{dr}{d\theta}\right)^2\right]^{\frac{1}{2}} d\theta. \tag{23}$$

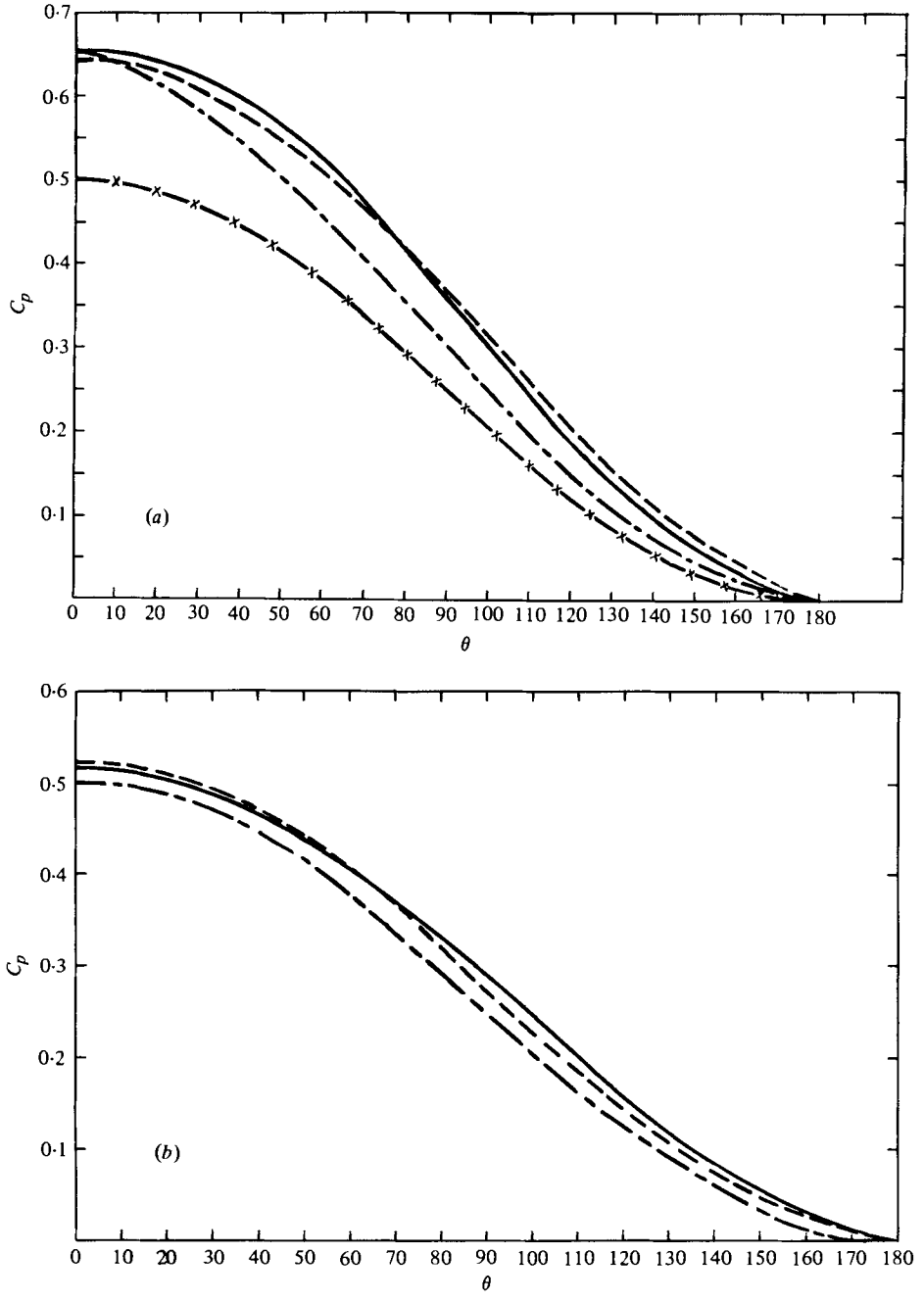

FIGURE 2. Surface pressure distribution for a paraboloid of revolution. (*a*) $Re_\infty = 10$: ——, first-order approximation; — · —, second-order boundary-layer theory; — — —, Davis & Werle (1972); — × —, potential flow around original body. (*b*) $Re_\infty = 100$: ——, Davis & Werle (1972); — · —, potential flow around original body; — — —, first-order approximation.

In the discussion beneath (6) it was mentioned that the pressure distributions as functions of distance along the original and displacement surfaces are equal to within an additive constant due to the viscous loss in total pressure along the stagnation streamline. In WKPG an expression for the increase in the wall pressure coefficient due to viscous losses is developed. This result, which is also valid for axisymmetric flow, is

$$C_{pw} = \frac{p_w - p_\infty}{\rho U_\infty^2} = \frac{1}{2}\left(1 + \frac{4}{Re}\frac{\partial V_e}{\partial y}\right), \tag{24}$$

where $\partial V_e/\partial y$ is the velocity gradient normal to the displacement thickness, and the Reynolds number is based on the radius of curvature R_0 at the forward stagnation point. For a paraboloid this is equal to twice the focal radius.

In figures 2(*a*) and (*b*) we have compared the results of the present approximate model with the numerical Navier–Stokes solutions of Davis & Werle (1972) for the surface pressure distribution on a paraboloid at a Reynolds number of 10 and 100. The importance of the viscous pressure losses predicted by (24) and the streamwise stretching of the body surface co-ordinate required by the pressure hypothesis (6) are particularly evident for the $Re = 10$ flow. The potential-flow pressure distribution for the inviscid flow past the original body considerably lags the Navier–Stokes solution for the surface pressure over the entire body. The inclusion of viscous-layer displacement effects using conventional axisymmetric boundary-layer theory to construct the displacement body and no co-ordinate stretching produces a curve which is nearly identical to the potential flow past the original body, while the inclusion of the viscous pressure losses from (24) serves only to elevate the surface pressure distribution in the region of the forward stagnation point. A very substantial improvement in the agreement with the exact Navier–Stokes solutions is achieved, however, with the first-order approximation to the displacement body obtained using the new pressure stretching hypothesis and the viscous correction for the pressure loss across the layer. The first-order approximation is obtained by curve fitting the zeroth-order displacement body using (19) and then mapping the pressure back to the body surface using (6). A typical curve fit employing 12 boundary points is able to generate a $\psi = 0$ boundary streamline which is nearly indistinguishable from the desired shape. Also shown in figure 2(*a*) for comparison is the pressure distribution obtained using second-order boundary-layer theory, a conventional construction of the displacement body and no co-ordinate straining.

5. Spheres

A much more rigorous test of the new approximate theory is the flow past a sphere in the Reynolds number range 5 to approximately 130, where a closed steady wake separation bubble is observed in both experiments and numerical Navier–Stokes solutions.

The solution scheme for spheres has already been described in detail in §3. Equation (10), when integrated using the surface velocity distribution (15), yields the first trial solution for the displacement body. This body is illustrated in figures 3(*a*) and (*b*) for an Re of 10 and 40. Also shown in these figures is the approximate solution for the inviscid flow past this displacement body obtained using (19) with $N = 2$, as discussed in §3.4. The four match points used are denoted by asterisks. The last

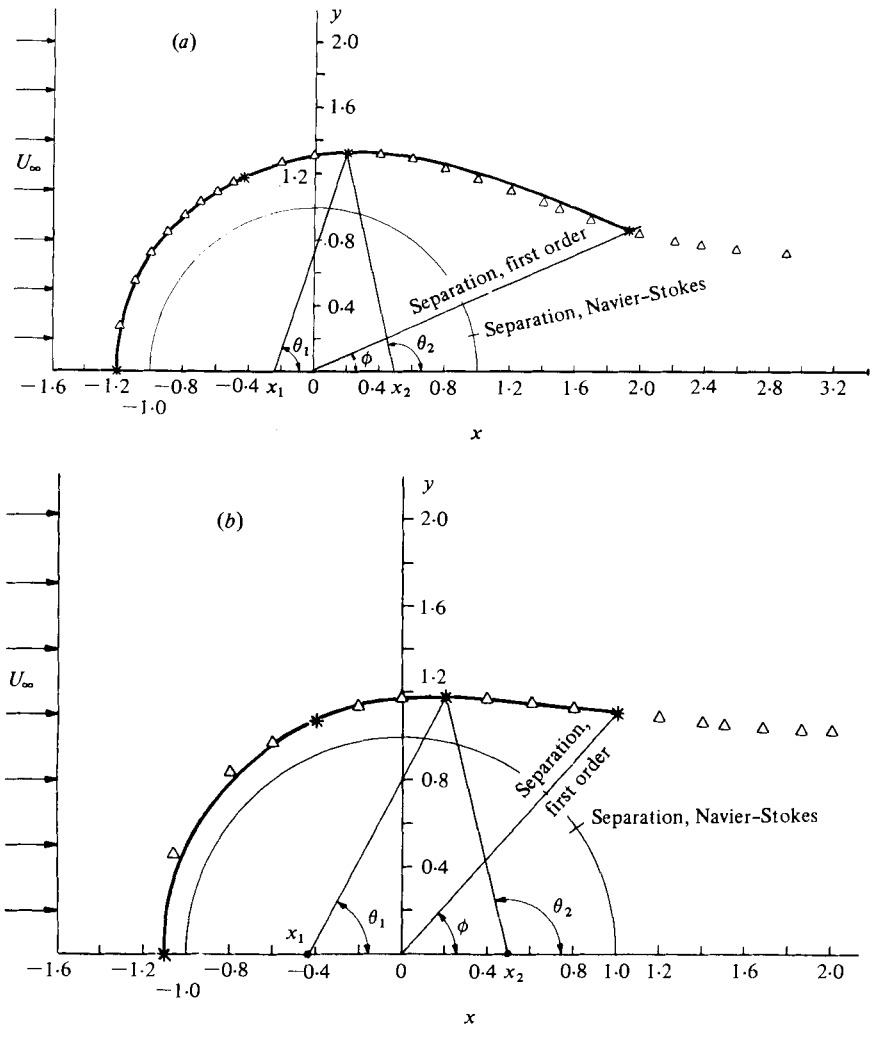

FIGURE 3. Stream-function fit of the displacement body for a sphere. ——, first-order approximation; △, stream-function fit; *, match points. (*a*) $Re_\infty = 10$. (*b*) $Re_\infty = 40$.

asterisk denotes the point of separation. The surprisingly good approximation that can be obtained for the displacement body using only two source–sink singularities is clearly evident in these figures.

Figures 4(*a*) and (*b*) show the displacement bodies obtained by the successive iteration procedure described in § 3.4. The significant deviation between the first- and higher-order approximations arises because the second- and higher-order approximations predict separation at a smaller angle ϕ from the rear stagnation point. This is shown in figure 5, where we have compared the theoretically predicted location of separation as a function of Reynolds number with available Navier–Stokes solutions. The difference between second- and higher-order approximate solutions is in general very small as observed in figures 4(*a*) and (*b*).

The crucial test of the new theory is whether it can accurately predict the surface pressure distribution on the sphere. Figures 6(*a*)–(*c*) illustrate the excellent com-

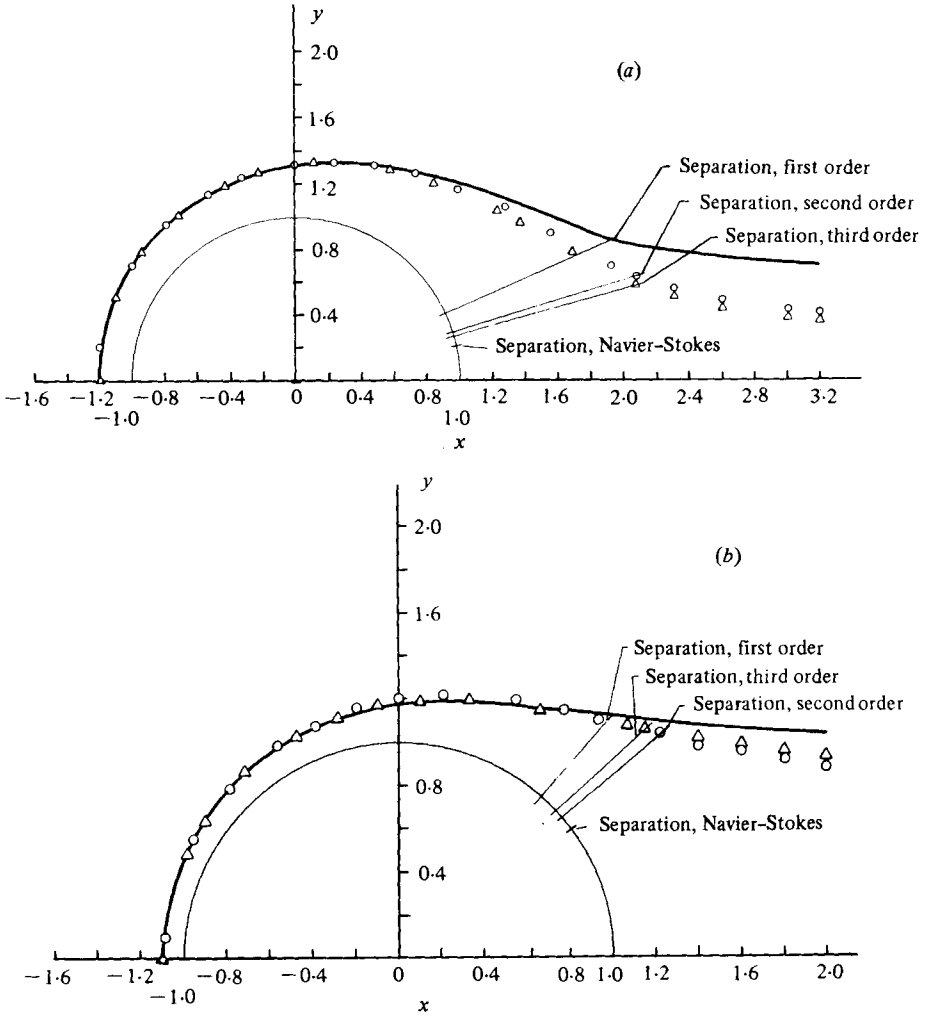

FIGURE 4. Successive approximations to the displacement body for a sphere. ——, first-order approximation; ○, second-order approximation; △, third-order approximation. (*a*) $Re_\infty = 10$. (*b*) $Re_\infty = 40$.

parison with available Navier–Stokes solutions obtained using the new pressure hypothesis (6). The pressure predicted by the new theory begins to deviate from the numerical Navier–Stokes solutions in the region just prior to separation. This could be due either to the assumptions involved in the derivation of the pressure hypothesis or to the failure of the quartic profile adequately to describe the flow in this region.

Also shown in these figures is the surface pressure predicted by second-order boundary-layer theory [equation (10)] and conventional construction of the displacement body. It was pointed out earlier that (10), in that it contains viscous corrections $O(\delta_0)$, is equivalent to the streamwise momentum equation used in second-order axisymmetric boundary-layer theory.

In table 2 we show the separation angles (as measured from the forward stagnation point) obtained for various Reynolds numbers by solving the conventional boundary-layer equation (10) without co-ordinate straining (second-order boundary-

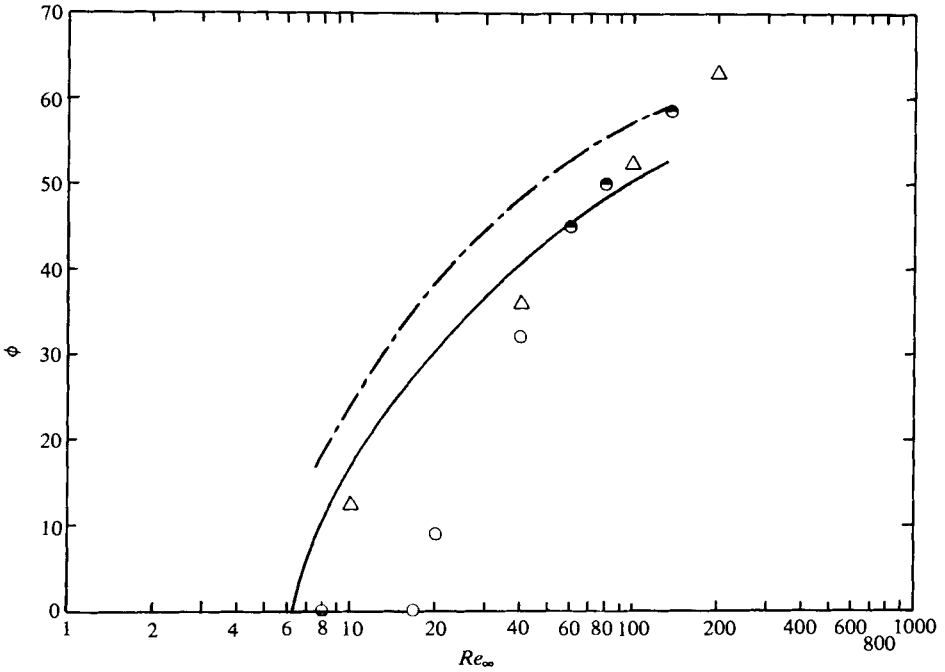

FIGURE 5. Separation angle as a function of Reynolds number for a sphere, — · —, first-order approximation; ——, second-order approximation. Numerical results: △, Rimon & Cheng (1969); ○, Jenson (1959). Experimental results: ◓, Taneda (1956); ◒, Nisi & Porter (1926).

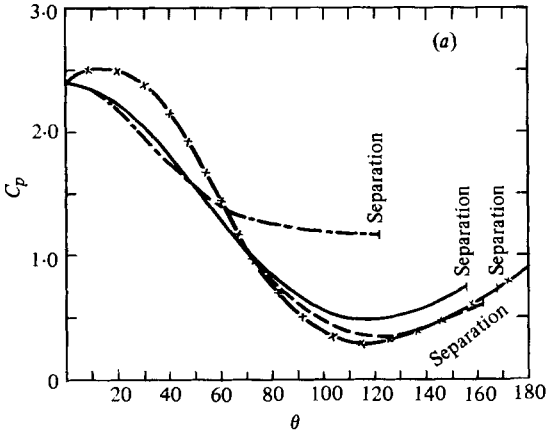

FIGURE 6(*a*). For legend see p. 598.

layer theory) and by solving (10) using the new pressure hypothesis. As may easily be seen from the table, the inclusion of just the higher-order viscous terms provides a small improvement over first-order axisymmetric boundary-layer theory when the conventional construction of the displacement body is used. At a Reynolds number of 100 (figure 6*c*) the higher-order curvature term in (10) provides a significant improvement in the predicted surface pressure without co-ordinate straining but a relatively poor prediction of the separation-point location. At a Reynolds number of 10 (figure 6*a*) the importance of the new pressure hypothesis is especially evident.

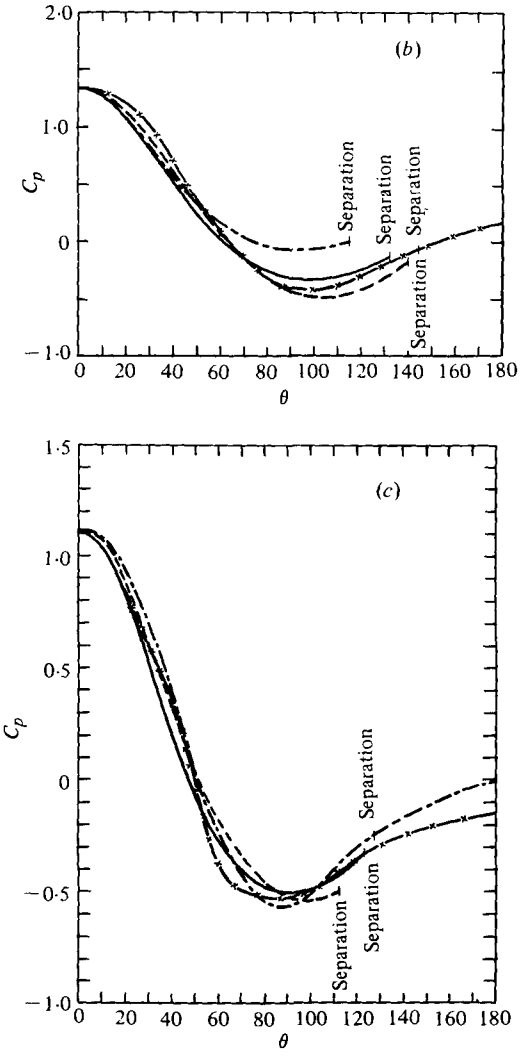

FIGURE 6. Surface pressure distribution around a sphere. (*a*) $Re_\infty = 10$. (*b*) $Re_\infty = 40$. (*c*) $Re_\infty = 100$. ——, first-order approximation. (*a*, *b*) — — —, second-order approximation; — · —, second-order boundary-layer theory; — × —, Rimon & Cheng (1969). (*c*) — — —, second-order boundary-layer theory; — · —, Rimon & Cheng (1969); — × —, Hamielec & Hoffman (1967).

In the present study we have been primarily concerned with determining the surface pressure up to the point of separation, since the fourth-order polynomial description given by (13) is a poor detailed representation of the flow in the separated region. The pressure at the rear stagnation point on the sphere could, therefore, not be used as the zero reference value as is commonly done in numerical Navier–Stokes solutions. Instead we have chosen the pressure at the forward stagnation point predicted by numerical Navier–Stokes solutions as the reference pressure for all sphere calculations.

The dramatic improvement over second-order boundary-layer theory in the prediction of the surface pressure distribution achieved using the new pressure

Reynolds number	Prandtl boundary-layer equations with conventional construction of displacement body	Second-order boundary-layer theory	Present theory, second-order approximation	Navier–Stokes solutions (Rimon & Cheng 1969)
10	115·9	121·7	163·0	167·5
20	113·4	118·4	150·0	
40	111·6	115·6	139·5	144
60	110·9	114·2	135·0	
100	109·98	112·9	130·0	127·5
130	109·61	112·2	127·5	
∞	109·6	109·6		

TABLE 2

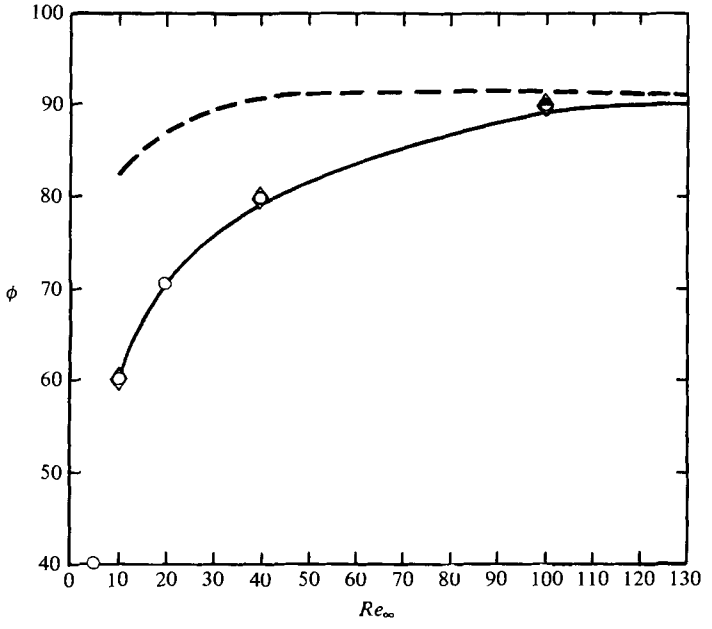

FIGURE 7. Angle of minimum surface pressure for a sphere. ——, second-order approximation; — — —, second-order boundary-layer theory; ◇, Rimon & Cheng (1969); ○, Jenson (1959); ◓, Hamielec & Hoffman (1967).

hypothesis (see figures 6*a*–c) can be attributed to the greatly improved representation of the first-order displacement body that results from the present solution procedure. In the conventional axisymmetric boundary-layer theory, where the first-order solution for the displacement body is based on the potential flow past the original body surface, separation occurs at approximately 109·6° from the forward stagnation point regardless of the Reynolds number. In contrast, the stretching of the body co-ordinate implicit in the new pressure hypothesis leads in the first trial solution

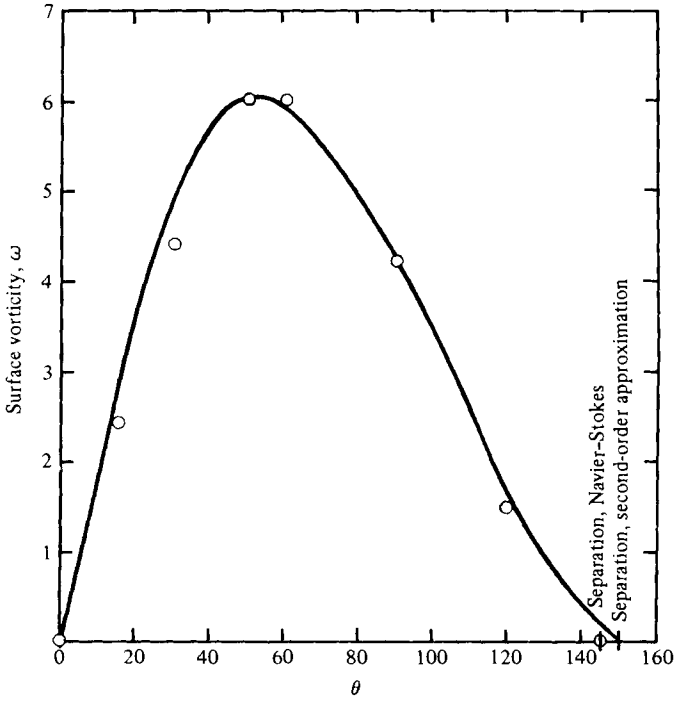

FIGURE 8. Surface vorticity distribution around a sphere. $Re_\infty = 40$. ——, second-order approximation; ○, Rimon & Cheng (1969).

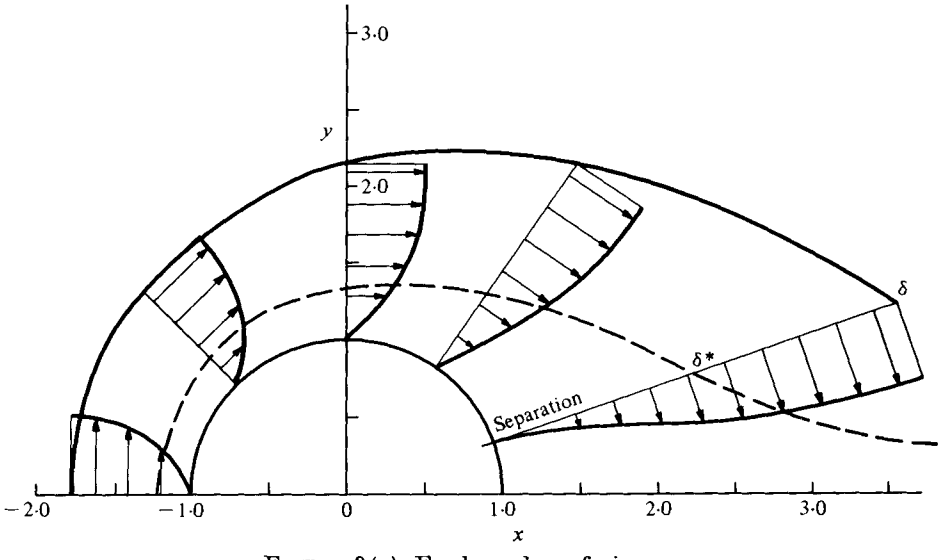

FIGURE 9(*a*). For legend see facing page.

to a reasonable prediction of the separation-point location as observed in figure 5. The importance of the new pressure hypothesis is clearly demonstrated in figure 7, where we have compared the angular locations of the minimum surface pressure predicted by second-order boundary-layer theory and the present approximate theory with available Navier–Stokes numerical solutions.

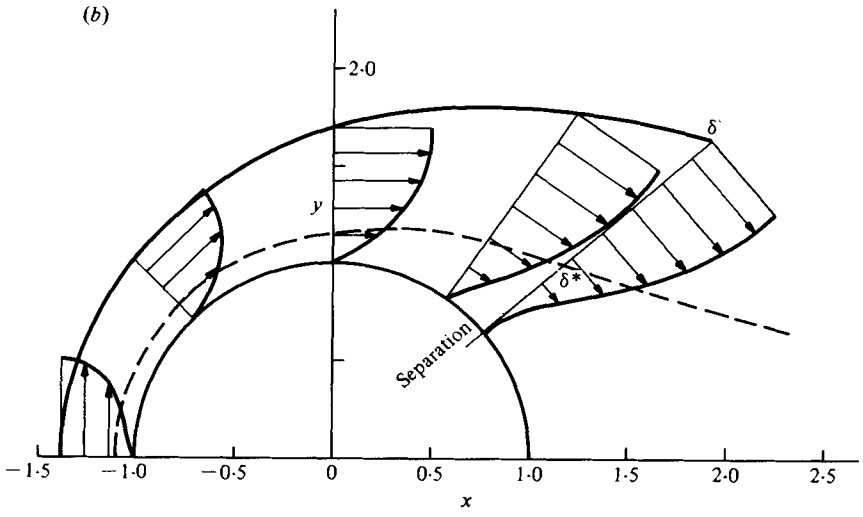

FIGURE 9. Velocity-profile development in the viscous layer around a sphere. (*a*) $Re_\infty = 10$. (*b*) $Re_\infty = 40$. — — —, displacement body, second-order approximation.

In figure 8 we show a typical surface vorticity distribution for the flow past a sphere at $Re = 40$. The agreement with exact Navier–Stokes solutions is excellent. Figures 9(*a*) and (*b*) show the velocity-profile development in the viscous layer and the growth of the boundary-layer outer edge up to separation at Reynolds numbers of 10 and 40 respectively. No difficulty is encountered in integrating the momentum-integral equation (10) through separation using the interaction pressure field. Thus if a more accurate family of separated flow profiles were constructed one should, in in theory, be able to obtain reasonable solutions for the wake separation bubble. This possibility is currently being studied.

6. Additional results and comments

The new theory has now been applied to a more general class of three-dimensional axisymmetric bodies: prolate spheroids, of which the sphere is a limiting case. These bodies are oriented such that their major axis is parallel to the flow. Figure 10 shows the displacement body obtained for a prolate spheroid of aspect ratio 10:9 (major/minor axis) at an Re of 100. Exact Navier–Stokes solutions due to Masliyah & Epstein (1970) exist for this case. Since this body shape is almost a sphere it was anticipated that a single source–sink pair would adequately model the displacement body. This proved to be the case, as can be seen in figure 10. Figure 11 compares the surface pressure distribution obtained using the new theory with the numerical Navier–Stokes solution of Masliyah & Epstein (1970). Figures 12 and 13 are for a prolate spheroid of aspect ratio 2:1. In this case it was necessary to use more boundary points (five) to obtain an adequate fit to the displacement body. The numerical solution of Masliyah & Epstein (1970) for the surface pressure distribution is shown in figure 13 for comparison.

In summary, the new proposed approximate theory described in WKPG and the present investigation has been shown to be in very good agreement with a broad

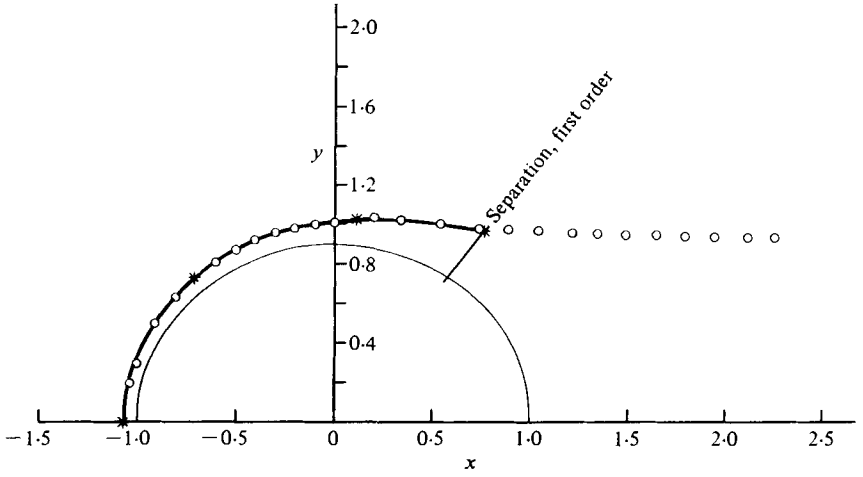

FIGURE 10. Stream-function fit of the displacement body for a prolate spheroid. $Re_\infty = 100$, aspect ratio = 10:9. ——, first-order approximation; ○, stream-function fit; *, match points.

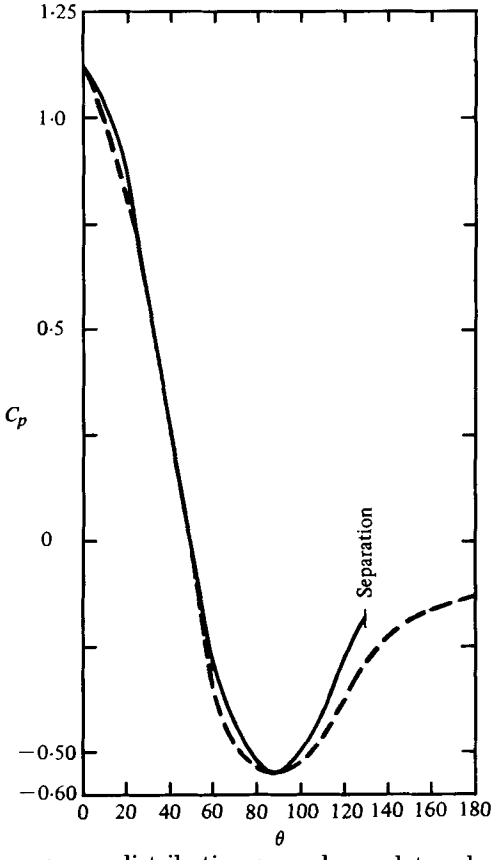

FIGURE 11. Surface pressure distribution around a prolate spheroid. $Re_\infty = 100$, aspect ratio = 10:9. ——, first-order approximation; — — —, Masiliyah & Epstein (1970).

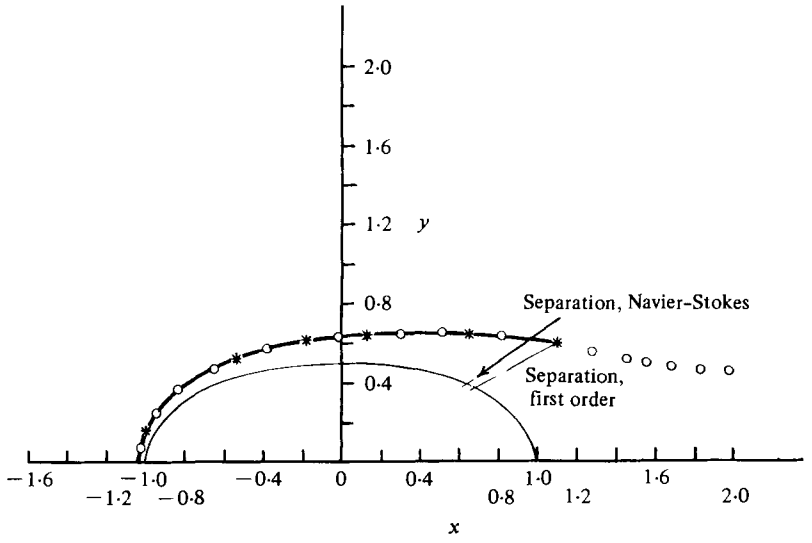

FIGURE 12. Stream-function fit of the displacement body for a prolate spheroid. $Re_\infty = 100$, aspect ratio = 2:1. ——, first-order approximation; ○, stream-function fit; *, match points.

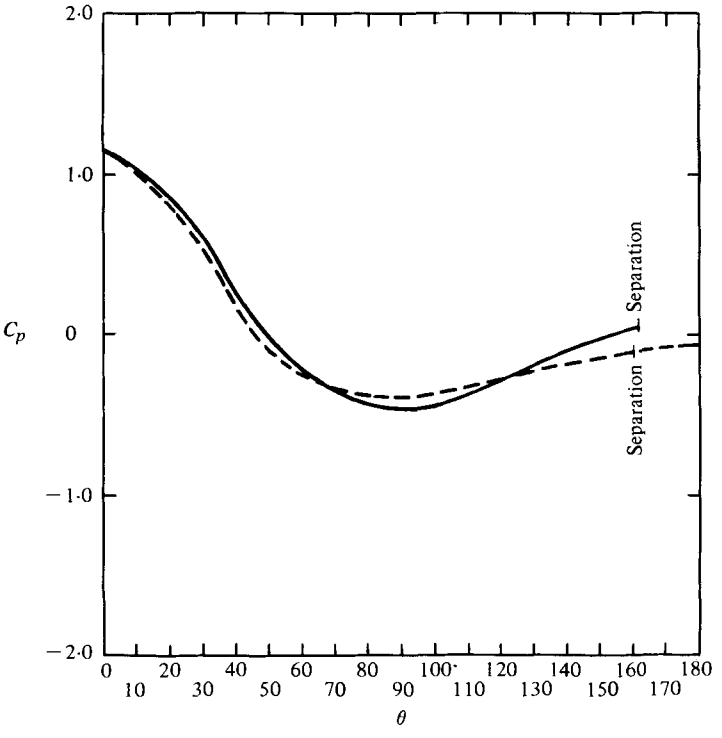

FIGURE 13. Surface pressure distribution around a prolate spheroid. $Re_\infty = 100$, aspect ratio = 2:1. ——, first-order approximation; — — —, Masiliyah & Epstein (1970).

spectrum of numerical Navier–Stokes solutions for the flow past smoothly contoured bodies in the intermediate Reynolds number range where the body is semi-infinite or finite with a steady laminar wake. The theory can be easily applied to many boundary shapes for which published numerical Navier–Stokes solutions currently do not exist. The important fundamental contribution of the study is the improved understanding of the role and construction of the displacement body and the effect of centrifugal forces in thick viscous layers.

This research was supported by the Office of Naval Research under contract NR-061-208. It was submitted in partial fulfilment of the requirements for a Ph.D. degree by Michael S. Kolansky. We gratefully acknowledge the assistance of Dr Michael J. Gluckman.

REFERENCES

BATCHELOR, G. K. 1967 *An Introduction to Fluid Dynamics.* Cambridge University Press.
DAVIS, R. T. & WERLE, M. J. 1972 *A.I.A.A.* **10**, 1224.
GLUCKMAN, M. J. 1971 Ph.D. thesis, The City University of New York.
HAMIELEC, A. E. & HOFFMAN, T. W. 1967 *A.I.Ch.E. J.* **13**, 212.
JENSON, W. G. 1959 *Proc. Roy. Soc.* A **249**, 346.
LIGHTHILL, M. J. 1958 *J. Fluid Mech.* **4**, 383.
MASILIYAH, J. H. & EPSTEIN, N. 1970 *J. Fluid Mech.* **44**, 493.
MILLIKAN, C. B. 1932 *Trans. A.S.M.E.* **54**, 29.
NISI, H. & PORTER, A. W. 1926 *Phil. Mag.* **46**, 754.
RIMON, Y. & CHENG, S. I. 1969 *Phys. Fluids* **12**, 949.
TANEDA, S. J. 1956 *J. Phys. Soc. Japan* **11**, 302.
VAN DYKE, M. 1962 *J. Fluid Mech.* **14**, 161.
WEINBAUM, S., KOLANSKY, M. S., PFEFFER, R. & GLUCKMAN, M. J. 1976 *Fluid Mech.* **77**, 129.
WERLE, M. J. & WORNOM, S. F. 1972 *Int. J. Engng Sci.* **10**, 875.